Research Square

Preprints are preliminary reports that have not undergone peer review.
They should not be considered conclusive, used to inform clinical practice,
or referenced by the media as validated information.

Multifunctional vortex magnetic tunnel junctions with optical and radio-frequency inputs for neuromorphic computing

Felix Oberbauer
Universität Greifswald
Tristan Joachim Winkel
Universität Greifswald
Clara C. Wanjura
Max Planck Institute for the Science of Light
Maksim Steblii
INL - International Iberian Nanotechnology Laboratory
John Justice
University College Cork
Jakob Walowski
Universität Greifswald
Tim Böhnert
INL - International Iberian Nanotechnology Laboratory
Eoin Russell
University College Cork
Farshad Moradi
University of Southern Denmark
Ricardo Ferreira
INL - International Iberian Nanotechnology Laboratory
Brian Corbett
University College Cork
Markus Münzenberg
Universität Greifswald
Tahereh Sadat Parvini
tahereh.s.parvini@gmail.com
Universität Greifswald

Article

Keywords:

Posted Date: November 11th, 2026

DOI: https://doi.org/10.21203/rs.3.rs-11448191/v1

License: This work is licensed under a Creative Commons Attribution 4.0 International License.
Read Full License

Additional Declarations: No competing interests reported.

Multifunctional vortex magnetic tunnel junctions with optical and radio-frequency inputs for neuromorphic computing

Felix Oberbauer,[1] Tristan Joachim Winkel,[1] Clara C. Wanjura,[2] Maksim Steblii,[3] John Justice,[4] Jakob Walowski,[1] Tim Böhnert,[3] Eoin Russell,[4] Farshad Moradi,[5] Ricardo Ferreira,[3] Brian Corbett,[4] Markus Münzenberg,[1] and Tahereh Sadat Parvini[1,6]

[1] *Institut für Physik, Universität Greifswald, 17489 Greifswald, Germany*
[2] *Max Planck Institute for the Science of Light, Staudtstraße 2, 91058 Erlangen, Germany*
[3] *INL - International Iberian Nanotechnology Laboratory, Avenida Mestre José Veiga, s/n, 4715-330 Braga, Portugal*
[4] *Tyndall National Institute, University College Cork, Cork T12 R5CP, Ireland*
[5] *ICELab, SDU Microelectronics, University of Southern Denmark, Denmark*
[6] *Walther-Meißner-Institut, Bayerische Akademie der Wissenschaften, Walther-Meißner-Str. 8, 85748 Garching, Germany*

The brain co-locates memory and processing, but many neuromorphic devices need standby power or separate memory from nonlinear computation. Here we show that vortex magnetic tunnel junctions with a non-volatile, thermally programmable storage layer provide two complementary nonlinear channels in one nanopillar. The laser-induced voltage is linear in laser power but cubic in direct-current bias, making the bias current a nonlinear, programmable weight, whereas radio-frequency excitation is rectified into a frequency-dependent voltage. Crossbar simulations using measured responses classify handwritten digits with 95.4% accuracy using optical inputs and 94.9% using radio-frequency inputs, comparable to an equal-size digital single-layer network. Microlenses focusing light to sub-micrometre spots, one formed directly on a junction, and a flip-chip-mounted vertical-cavity surface-emitting laser array provide a route to on-chip optical addressing. Operating both channels together could combine optical and radio-frequency inputs within one nanoscale device, making vortex junctions reprogrammable multi-input building blocks for analog neuromorphic hardware.

Corresponding authors: Markus Münzenberg (email: muenzenbem@uni-greifswald.de) and Tahereh Sadat Parvini (email: tahereh.s.parvini@gmail.com)

I. INTRODUCTION

The growing energy and data-movement costs of modern artificial intelligence have intensified interest in neuromorphic computing as a hardware route toward brain-inspired, energy-efficient information processing. By co-locating memory and computation in adaptive physical elements, neuromorphic architectures can mitigate the von Neumann bottleneck that constrains conventional transistor-based systems, particularly for inference workloads that require massive parallelism and low-latency analog operations [1–5]. Realizing this promise requires nanoscale devices that combine non-volatility, tunability, a strong nonlinear response and low-power operation within a single element. Spintronic devices are particularly well suited to this role: magnetic tunnel junctions (MTJs), MTJ-based spin-torque nano-oscillators (STNOs) and spin Hall nano-oscillators (SHNOs) offer compact footprints, compatibility with complementary metal–oxide–semiconductor (CMOS) back-end processing, and rich magnetization dynamics that can provide both computational nonlinearity and memory [6–12]. Among them, vortex-based STNOs are especially attractive: their topologically protected vortex core is robust, and the gyrotropic mode of the core provides a smooth yet strongly nonlinear analog response [13–15] that has been exploited in reservoir computing and coupled-oscillator networks [16–21].

While vortex oscillators provide the nonlinear dynamics required for analog neuromorphic computing, their use in reconfigurable hardware depends on persistent, non-volatile control of the oscillator operating point. Martins *et al.* showed that an electrically set vortex chirality, retained after the initializing signals are removed, can act as a binary non-volatile synapse read out through the spin-torque diode effect [22]. Stebliy *et al.* extended this concept to continuous analog tuning by integrating a ferromagnet/antiferromagnet (NiFe/IrMn) exchange-bias storage layer into the MTJ nanopillar: Joule heating by a voltage pulse raises the antiferromagnet above its blocking temperature, and subsequent field cooling resets the exchange-bias direction, which displaces the vortex-core equilibrium and shifts the gyrotropic frequency persistently over a ∼15 MHz range without continuous power dissipation [23]. This scheme provides a continuously tunable, non-volatile operating point, but it is addressed only electrically. A complementary, non-contact input channel is offered by spin caloritronics [24–26]: laser-induced temperature gradients across MgO tunnel barriers generate tunnel magneto-Seebeck (TMS) voltages whose sign and magnitude depend on the magnetic configuration, as established in CoFeB/MgO/CoFeB junctions [27, 28] and enhanced in optimized material systems [29].

Under an additional dc bias, the laser-induced voltage becomes strongly bias dependent in the bias-enhanced TMS (bTMS) regime [30]. We recently showed that this bias dependence is well described by a cubic polynomial and can serve as the nonlinear element of simulated crossbar networks, which reached 93.7% accuracy in handwritten-digit classification [31]; those junctions, however, had no storage layer and used only the optical input channel. Vortex MTJs also support a second nonlinear transduction mode, the spin-torque diode effect [32, 33], in which radio-frequency (RF) excitation near the gyrotropic resonance is rectified into a dc voltage; such rectification has been used for neuromorphic and RF signal processing [34, 35]. To our knowledge, however, thermoelectric transport has not yet been studied in storage-layer vortex MTJs, and the thermoelectric and spin-diode nonlinearities have not been combined on one non-volatile, reprogrammable device platform.

Here we combine these ingredients in CoFeB/MgO/CoFeB vortex MTJs with an integrated IrMn-based storage layer and report four advances. First, we show, to our knowledge for the first time, that storage-layer vortex junctions exhibit a reproducible TMS response under laser heating, measured on nine junctions: the thermovoltage is linear in laser power and switches between the parallel and antiparallel states, and under dc bias the laser-induced voltage follows a cubic polynomial, so that the bias current acts as a nonlinear, programmable weight for the optical input. Second, using the measured thermoelectric and spin-diode response maps, we simulate crossbar networks in two operating modes on the same non-volatile hardware platform. The optical (bTMS) mode reaches 95.4% handwritten-digit classification accuracy, compared with 93.7% for our earlier junctions on the same task and network size [31], and the RF (spin-diode) mode reaches 94.9%; both are comparable to a digital single-layer network of the same size, and in the optical mode smaller junctions with a stronger bias dependence perform better. Third, we propose a combined operating mode in which simultaneous optical, dc and RF driving generates cross-terms between optical and RF inputs within one device, an interaction between inputs that conventional in-memory computing arrays cannot compute directly, and we identify the physical couplings that produce it. Fourth, we fabricate microlenses that focus light to sub-micrometre spots, form such a lens directly on a nanopillar device and flip-chip mount a vertical-cavity surface-emitting laser (VCSEL) array, the first steps towards on-chip optical addressing of magnetic tunnel junctions. Finally, we place the energy and compute density of the platform in the context of existing neuromorphic hardware.

II. DEVICE FEATURES AND OPTO-ELECTRICAL MEASUREMENT SETUP

Our devices are vortex spin-transfer torque nano-oscillators (STNOs) based on magnetic tunnel junction (MTJ) nanopillars with diameters of 600, 800, and 1000 nm, fabricated at the International Iberian Nanotechnology Laboratory (INL) in the same run as the devices of ref. [23] (Fig. 1a–c; Methods). The device platform and spin-diode characterization build on our previously reported non-volatile frequency-programmable vortex MTJ architecture [23]. The magnetic stack comprises three functional subsystems. An $Ir_{20}Mn_{80}$ antiferromagnet [AFM1, $T_B^{AFM1} \approx 230\,^{\circ}C$] exchange-biases the synthetic antiferromagnet (SAF) reference layer [$Co_{70}Fe_{30}$/Ru/$Co_{40}Fe_{40}B_{20}$], providing a thermally stable fixed magnetization reference during device operation. The free layer [$Co_{40}Fe_{40}B_{20}$/Ta/NiFe] hosts a magnetic vortex state and is separated from the SAF by an MgO tunnel barrier, yielding a tunnel magnetoresistance ratio of ∼100–120% (ref. [23] and Supplementary Note 4) and a resistance–area product of $\sim 10\,\Omega\,\mu m^2$ [23]. The reconfigurable storage layer [NiFe/$Ir_{20}Mn_{80}$] (AFM2, $T_B^{AFM2} \approx 180\,^{\circ}C$) is positioned 10 nm above the free layer via a non-magnetic Cu spacer, generating a tunable magnetostatic stray field that modulates the free-layer vortex dynamics without direct exchange coupling. Both blocking temperatures were measured on continuous films (Methods). The $\sim 50\,^{\circ}C$ separation between T_B^{AFM1} and T_B^{AFM2} defines a selective thermal operating window for non-volatile reconfiguration: voltage pulses (0.9 V, 1 ms) generate Joule heating that raises AFM2 above T_B^{AFM2} while leaving AFM1, and therefore the SAF reference, pinned. The storage-layer magnetization then relaxes under an applied reconfiguration field B_{REC} and freezes upon cooling, enabling either a saturated single-domain state or a displaced vortex-like configuration with a tunable magnetostatic bias. The resulting storage-layer stray field, obtained from micromagnetic simulations (Methods), is tunable over approximately ±5 mT (Fig. 1d), and was shown previously to shift the free-layer gyrotropic resonance frequency continuously over a ∼ 15 MHz range in a fully non-volatile manner for 600 nm devices [23]. The nonlinear device response central to this work is directly evidenced by the spin-torque diode effect, in which an incident RF signal drives gyrotropic precession of the vortex core and the oscillating tunnel magnetoresistance rectifies the response into a DC voltage. Because the rectified amplitude depends nonlinearly on the detuning between the excitation frequency and the vortex resonance, the device naturally implements a compact analog transfer function—analogous to a neuromorphic activation function—without additional circuitry. Fig. 1f presents this rectified voltage for a 600 nm device of the same fabrication run [23] at nominally zero applied field ($B_{ext} \approx 0$) for two RF excitation powers (−10 dBm and −5 dBm), where the pronounced nonlinearity is clearly visible and directly exploited for neuromorphic processing in this work.

In this work, we optically heat the MTJs and read out the resulting thermoelectric voltages, complementing the non-volatile reconfiguration reported in Ref. [23]. Each junction is electrically selected and heated individually by a

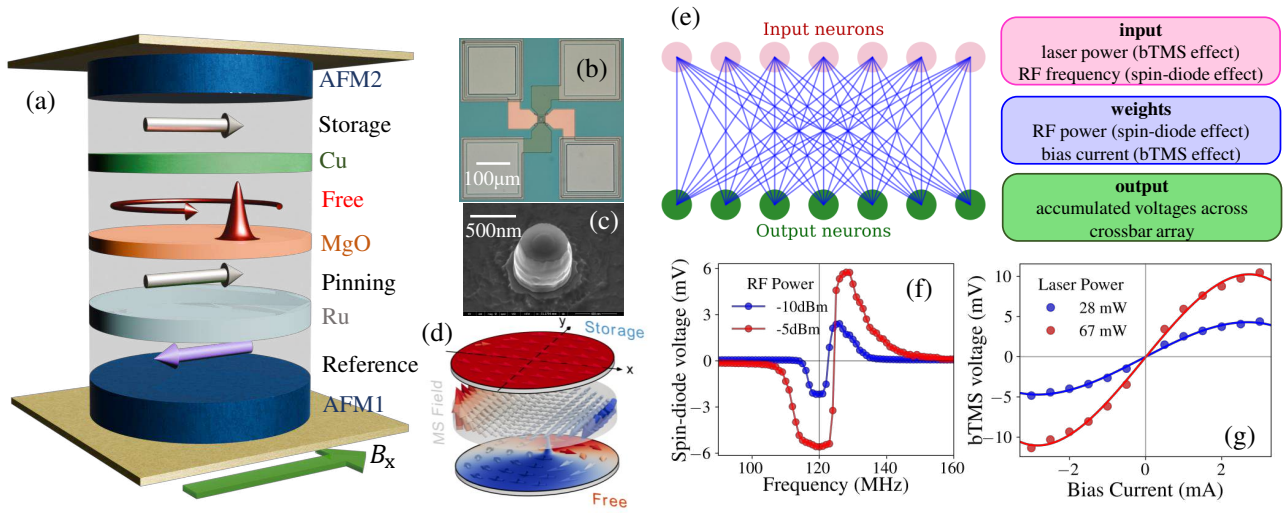


FIG. 1. **Device concept and nonlinear response characteristics enabling neuromorphic functionality.** (a) Schematic representation of the studied structure. (b) Optical microscope image of the structure. (c) Scanning electron microscopy (SEM) image of the MTJ nanopillar. (d) Distribution of the magnetostatic field generated by the storage layer and acting on the free layer, obtained from micromagnetic simulations (MuMax3). (e) Schematic representation of a neural-network layer and the physical quantities that take the roles of input, output, and weights: in the case of the bTMS effect, the input is injected optically while synaptic weights are controlled with bias currents; in the case of the spin-diode effect, the input is encoded in the frequency of an RF signal while its power plays the role of a synaptic weight. In the bTMS case, the cubic bias dependence makes the bias current a nonlinear, programmable weight; in the spin-diode case, the response is nonlinear in the input frequency, playing a role analogous to an activation function. (f) Measured spin-diode response under RF excitation (data from ref. [23]), showing a strongly nonlinear voltage characteristic that directly supplies a rich analog transfer function for neuromorphic signal processing. (g) Measured bias-enhanced tunnel magneto-Seebeck (bTMS) voltage versus dc bias current for two laser powers, highlighting the pronounced cubic bias dependence that sets a nonlinear, programmable weight.

modulated, focused laser (Methods), so these measurements probe the optothermal response of individual devices rather than simultaneous array operation. The 600–1000 nm nanopillar diameter and the optical input resolution are different length scales. The former defines the physical MTJ size, whereas the latter is set by the 7 μm free-space laser spot and heat spreading in the multilayer stack. The present experiment therefore demonstrates optothermal actuation of individually contacted nanoscale MTJs, but not independent optical addressing at the nanopillar pitch. In future optically driven arrays, the addressable pitch will be determined by optical focusing, absorption profile, lateral heat diffusion, and thermal guard spacing between neighbouring junctions (Sec. V). Unlike ultrafast pulsed optical excitation, in which photons couple directly to the magnetic order [36, 37], the CW illumination employed here acts exclusively as a thermal actuator via optical absorption and electron–phonon thermalization, leaving the magnetic configuration unperturbed. Within each modulation half-cycle, a quasi-steady thermal profile establishes a steep temperature gradient ΔT across the MgO barrier. Heat transport through the barrier is dominated by phonons rather than electrons, whose thermal conductance estimated via the Wiedemann–Franz law is orders of magnitude smaller [38, 39]. The barrier therefore acts as a thermal bottleneck: thin sputtered MgO films have a thermal conductivity of about 3.6 $\mathrm{W\,m^{-1}K^{-1}}$ [38], roughly an order of magnitude below single-crystal MgO ($\sim$48 $\mathrm{W\,m^{-1}K^{-1}}$) due to grain-boundary and defect scattering, and 2-nm barriers including their CoFeB/MgO interfaces have an effective thermal conductivity of only 0.4–0.6 $\mathrm{W\,m^{-1}K^{-1}}$ [39]. The interfaces therefore dominate the thermal resistance of the barrier, so that a sizeable temperature drop develops across it [40]. The resulting ΔT asymmetrically broadens the Fermi–Dirac distribution in the heated electrode relative to the cold side. This energy-dependent carrier imbalance, filtered by the MTJ's spin- and energy-selective transmission function $T(E)$, generates a thermoelectric voltage whose magnitude is governed by the logarithmic energy derivative of $T(E)$ at the Fermi level [27, 41, 42]. Under open-circuit, small-signal conditions, the first-harmonic response at the modulation frequency obeys $V^{\mathrm{AC}}_{\mathrm{P/AP}} = S_{\mathrm{P/AP}}\,\Delta T$, where the Seebeck coefficients S_{P} and S_{AP} of the parallel (P) and antiparallel (AP) states differ because they reflect the spin-dependent electronic structure near the Fermi level [27, 29, 43]; this is the tunnel magneto-Seebeck (TMS) effect.

Applying a dc bias shifts the electrochemical potentials of the electrodes and reshapes the tunnelling window, which imparts an explicit bias dependence to the first-harmonic response through the bias-modified transmission; this defines the bias-enhanced TMS (bTMS) regime [26, 30]. Within the Onsager linear-response framework [44, 45], the thermal and electrical drives enter as independent thermodynamic forces; the pronounced bias nonlinearity observed in the

bTMS regime arises from the bias-dependent tunnelling transmission and higher-order transport contributions beyond strict linear response.

Two distinct timescales govern device operation. Programming writes the storage-layer configuration with the Joule-heating pulse described above; once programmed, the state is retained without standby power and is not rewritten during inference. Inference reads the programmed junction through the bTMS or the spin-diode channel, so the programming time sets the latency of weight updates, whereas the inference speed is set by the readout bandwidth of the operating mode: in the spin-diode mode, the rectified voltage builds up within the damping time of the gyrotropic mode, $1/(\pi\Delta f) \approx 0.03$–$0.3$ μs for linewidths Δf of 1–10 MHz at gyrotropic frequencies of 125–142 MHz [23]. The 1 kHz cadence of the present bTMS measurements reflects the optical modulation and lock-in detection, not repeated programming.

III. EXPERIMENTAL RESULTS AND DISCUSSION

To probe the TMS effect in the STNOs, we performed open-circuit magnetic-field sweeps while varying the laser power (Methods). The loops show hysteretic switching between distinct voltages $V_{\mathrm{P}}^{\mathrm{AC}}$ and $V_{\mathrm{AP}}^{\mathrm{AC}}$. We quantify the thermoelectric contrast using the TMS ratio, defined analogously to the tunnel magnetoresistance (TMR) ratio [46, 47],

$$\mathrm{TMS} = \frac{S_{\mathrm{AP}} - S_{\mathrm{P}}}{\min(|S_{\mathrm{AP}}|, |S_{\mathrm{P}}|)} \equiv \frac{V_{\mathrm{AP}}^{\mathrm{AC}} - V_{\mathrm{P}}^{\mathrm{AC}}}{\min\left(|V_{\mathrm{AP}}^{\mathrm{AC}}|, |V_{\mathrm{P}}^{\mathrm{AC}}|\right)}. \tag{1}$$

Figure 2(a–c) displays $V^{\mathrm{AC}}(B)$, with switching fields consistent with the TMR characterization (Supplementary Note 3). Figure 2(d–f) summarizes the power dependence of $V_{\mathrm{P}}^{\mathrm{AC}}$, $V_{\mathrm{AP}}^{\mathrm{AC}}$, their voltage contrast $\delta V_{\mathrm{P,AP}} = V_{\mathrm{AP}}^{\mathrm{AC}} - V_{\mathrm{P}}^{\mathrm{AC}}$, and the TMS ratio. For the representative devices shown, $V_{\mathrm{P/AP}}^{\mathrm{AC}}$ varies linearly with laser power, consistent with a steady-state temperature rise $\Delta T \propto P_{\mathrm{abs}}$ and approximately constant $S_{\mathrm{P/AP}}$ over the modest heating range [27, 29]. The resulting signals are in the μV range [27, 29] and are readily resolved by lock-in detection. Because the response remains linear, the signal can be increased without altering the transport regime; for example, transparent ITO top contacts have been shown to raise thermovoltages into the mV range at comparable laser powers by improving optical coupling to the stack [31]. More generally, continuous optical tunability provides a practical non-contact analog control parameter relevant for neuromorphic input encoding, reconfigurable spintronic logic, and thermal sensing. Device-to-device reproducibility across nine junctions and the repeatability of laser-power sweeps over several months are documented in Supplementary Note 1.

The TMS ratio and the voltage contrast $\delta V_{\mathrm{P,AP}} = (S_{\mathrm{AP}} - S_{\mathrm{P}})\,\Delta T$ exhibit the opposite diameter dependence, with smaller pillars systematically yielding larger values: the mean TMS ratios are $125 \pm 28\%$, $77.0 \pm 7.5\%$ and $54.5 \pm 4.4\%$ for $d = 600$, 800 and 1000 nm (mean $\pm$ s.d. over three devices each; Supplementary Note 1). Because ΔT cancels in the TMS ratio, this trend cannot be explained by a diameter-dependent temperature difference and must originate in the Seebeck coefficients themselves. A plausible origin is electronic and relates to coherent spin filtering in the MgO barrier. In sputtered polycrystalline MgO, grain boundaries and structural disorder introduce additional, less spin-selective tunneling channels that partially bypass the coherent Δ_1 symmetry-filtered transport responsible for both high TMR and large Seebeck contrast [48, 49]. Larger junctions are statistically more likely to contain such defective regions, which reduces the effective contrast $S_{\mathrm{AP}} - S_{\mathrm{P}}$. Consistent with this picture, the TMR is also larger in smaller pillars, reaching $\sim$120% at $d = 600$ nm compared with $\sim$105% at $d = 800$ nm (Supplementary Note 4). The slight increase of $|V_{\mathrm{P/AP}}^{\mathrm{AC}}|$ with diameter, also reported by Böhnert *et al.* [50] for junctions embedded in Al_2O_3, suggests that ΔT itself does not decrease with diameter. A quantitative separation of thermal and electronic contributions would require finite-element extraction of $\Delta T(d)$ combined with transport modelling that captures realistic barrier disorder; this is beyond the scope of the present work.

Under simultaneous heating and bias, the lock-in detected laser on/off voltage difference $\Delta V_{\mathrm{AC}}^{\mathrm{P/AP}} \equiv V_{\mathrm{AC,on}}^{\mathrm{P/AP}} - V_{\mathrm{AC,off}}^{\mathrm{P/AP}}$ obeys

$$\Delta V_{\mathrm{AC}}^{\mathrm{P/AP}} = S_{\mathrm{P/AP}}\,\Delta T + \left(R_{\mathrm{P/AP}} - \Delta R_{\mathrm{P/AP}}\right) I - R_{\mathrm{P/AP}} I, \tag{2}$$

where $R_{\mathrm{P/AP}}$ is the resistance of the unheated STNO and $\Delta R_{\mathrm{P/AP}}$ denotes the resistance change induced by laser heating in the P and AP states (Supplementary Note 5). To quantify the switching contrast, we define the bTMS ratio as

$$\mathrm{bTMS} = \frac{\Delta V_{\mathrm{AC}}^{\mathrm{AP}} - \Delta V_{\mathrm{AC}}^{\mathrm{P}}}{\min\left(\left|\Delta V_{\mathrm{AC}}^{\mathrm{P}}\right|,\ \left|\Delta V_{\mathrm{AC}}^{\mathrm{AP}}\right|\right)}. \tag{3}$$

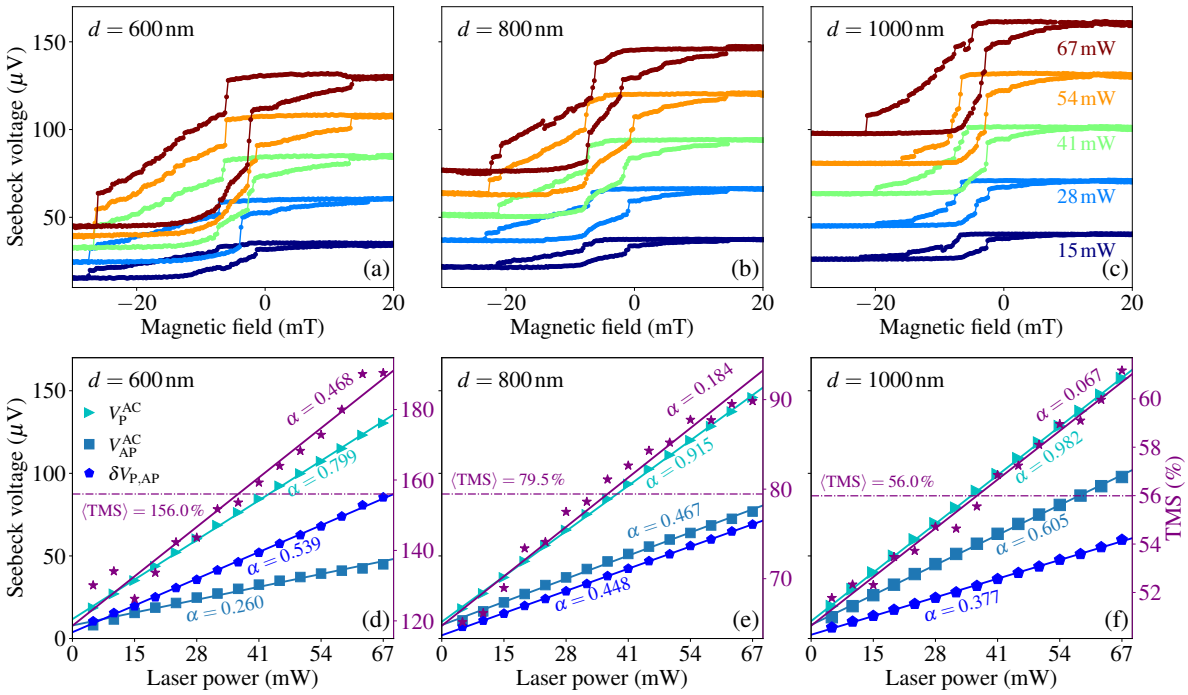


FIG. 2. **Laser-induced tunnel magneto-Seebeck effect in vortex spin-torque nano-oscillators.** (a–c) Zero-bias Seebeck voltage V^{AC} as a function of in-plane magnetic field $B_\parallel$ for nanopillars with diameters $d = 600$, 800, and 1000 nm, measured for laser powers at the sample $P = 15$–67 mW. (d–f) Power dependence of the Seebeck voltages in the parallel and antiparallel configurations, V_P^{AC} and V_{AP}^{AC}, evaluated at $B_\parallel = \pm 30$ mT, together with their difference $\delta V_{P,AP} = V_{AP}^{AC} - V_P^{AC}$ and the TMS ratio. Solid lines are linear fits; the corresponding slopes α are given in μV mW^{-1} for the voltage traces and in % mW^{-1} for the TMS ratio. Dashed purple lines mark the mean TMS ratio.

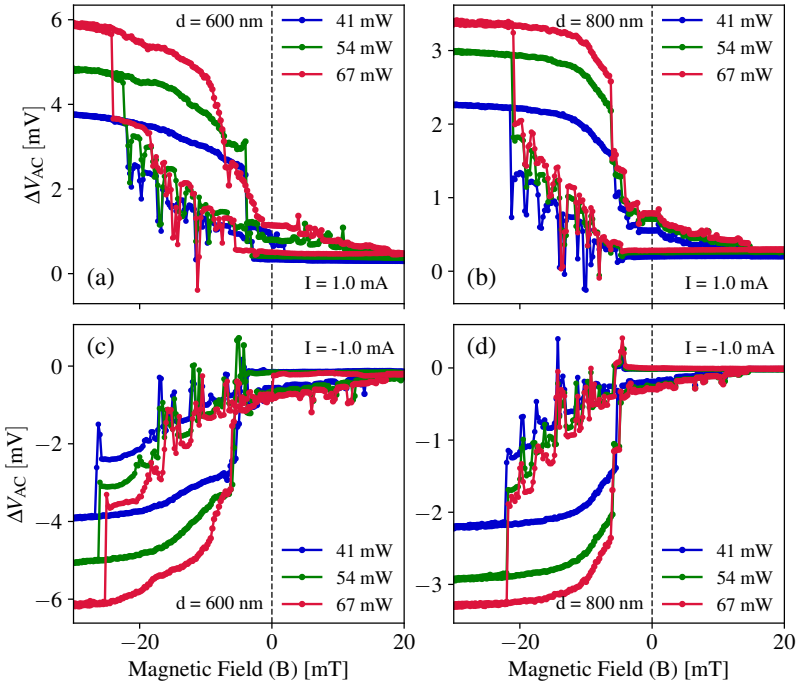


FIG. 3. **Laser-induced voltage ΔV_{AC} as a function of in-plane magnetic field B.** (a,b) Vortex STNOs with $d = 600$ nm and (c,d) $d = 800$ nm. The data were acquired with a magnetic-field step of 0.25 mT.

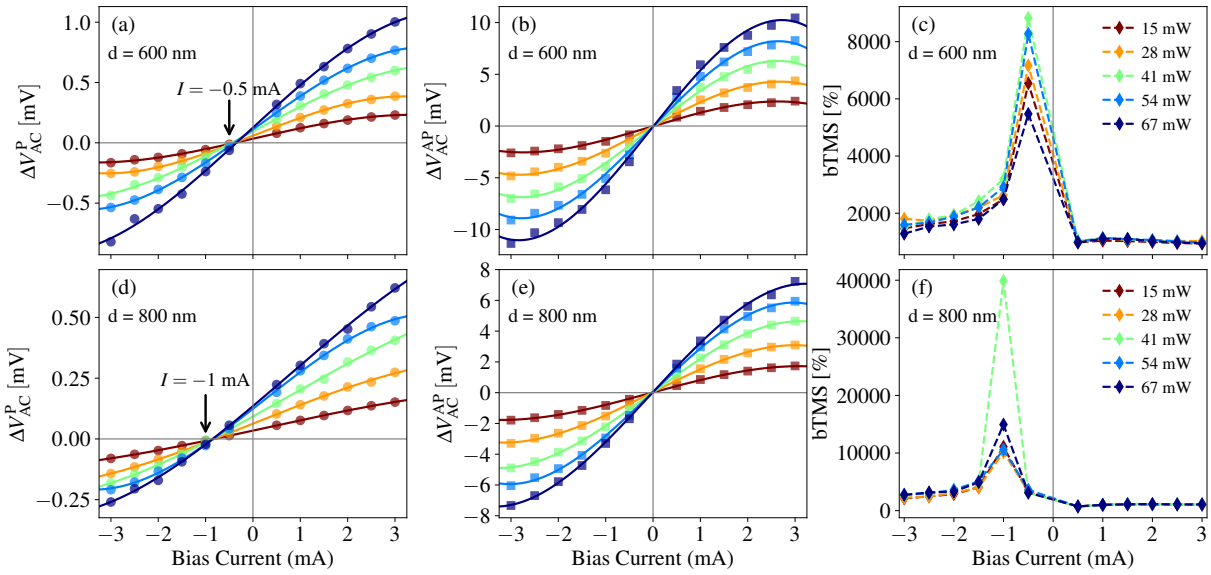


FIG. 4. **Measured laser-induced voltage in the P and AP states as well as bTMS ratio as a function of bias current for individual laser powers.** Vortex STNO devices with nanopillar diameters $d = 600$ nm (top row) and $d = 800$ nm (bottom row). Solid lines in (a), (b), (d), and (e) represent cubic polynomial fits to the data of the form $V(I) = \sum_{n=0}^{3} a_n I^n = a_3 I^3 + a_2 I^2 + a_1 I + a_0$, while the curves in (c) and (f) serve as guides to the eye.

As shown in Supplementary Note 3 and Supplementary Fig. 9, the resistance and the laser-induced voltage ΔV_{AC} switch at the same magnetic field, confirming their shared magnetic origin; the junction remains bistable (P/AP), but the combined readout $(R, \Delta V_{\mathrm{AC}})$ provides two independent signals of the same magnetic state, carried by charge transport and by the thermoelectric response. A particularly striking feature is the appearance of Barkhausen jumps in resistance [51, 52], which manifest as sharp spikes in ΔV_{AC} (Fig. 3) and are likely associated with vortex-core transitions [53]. According to Eq. (2), such spikes are predominantly driven by abrupt changes in $\Delta R_{\mathrm{P/AP}}$, and the stray field of the storage layer, which alters vortex-core stability and domain-wall pinning, further influences them. If confirmed by time-resolved measurements, which are needed to exclude lock-in transients and to resolve pinning–depinning events, these transient thermoelectric responses could provide a spike-based signalling pathway for event-driven neuromorphic computing and spintronic reservoir computing.

Figure 4 shows the first-harmonic laser-induced voltage $\Delta V_{\mathrm{AC}}(I)$ as a function of bias current for several laser powers in the P and AP states, together with the bTMS ratio. Unlike the zero-bias TMS regime, the bTMS voltages are nonlinear in I and are well captured by a cubic polynomial, consistent with the third-order cross-term expected from the Landauer–Büttiker framework [30, 31]: because the tunnel conductance varies approximately quadratically with bias [54], the heating-induced resistance change ΔR acquires a term in I^2, so that the resistive term $\Delta R\, I$ contains contributions linear and cubic in I. Notably, for $d = 600$ nm ($d = 800$ nm) at $I = -0.5$ mA ($I = -1.0$ mA), the near-vanishing $\Delta V_{\mathrm{AC}}^{\mathrm{P}}$ produces an exceptionally high bTMS ratio, demonstrating that bias tuning can deliver readout contrasts far beyond those accessible by TMR alone [30]. Run-to-run and device-to-device reproducibility of the bTMS response in Fig. 4 are documented in Supplementary Note 2. At fixed bias, ΔV_{AC} grows linearly with laser power (Supplementary Note 6), so each junction multiplies its optical input by an effective weight that is set nonlinearly by the bias current.

IV. PROPOSAL FOR EFFICIENT NEUROMORPHIC COMPUTING

The neuromorphic results reported below are simulations parameterized by measured device responses rather than measurements on a fabricated crossbar: the bTMS and spin-diode response maps are measured, whereas array connectivity, training and classification are evaluated numerically. The simulations therefore test the computational potential of the measured device responses, not a complete system-level hardware implementation.

We recently proposed [31] that magnetic tunnel junctions could serve as a flexible and scalable neuromorphic computing platform, in which a crossbar array carries out the multiply–accumulate operation with device-level nonlinear weights in a single physical step [55]. Here we extend this concept to two operating modes on the same

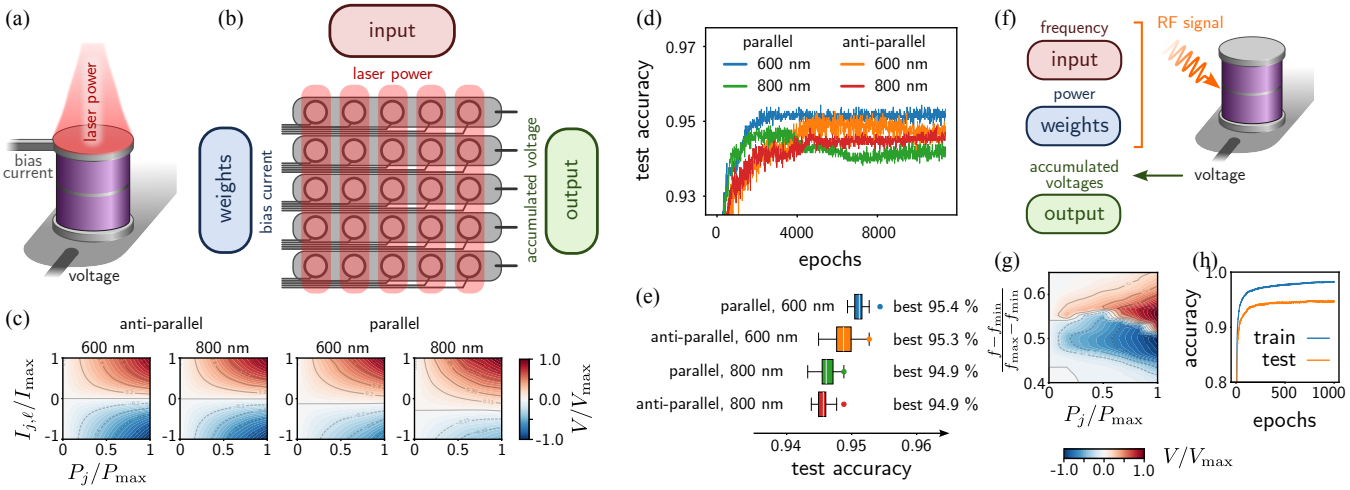


FIG. 5. **Neuromorphic computing performance for different device dimensions and operations.** (a) We leverage the nonlinear response due to the bTMS effect. The laser power is used to encode the input data, while the bias currents implement synaptic weights. (b) A crossbar-array architecture performs the multiply–accumulate operation with device-level, bias-programmable weights in one step. Input powers are set equal across a column, and output voltages are accumulated along a row to yield the output of the neural network layer. (c) We use interpolation functions (4) that interpolate linearly between measurement data points to realistically model the device response. We consider different device sizes and operation modes. (d) The evolution of the test accuracy during the training. Smaller devices attain a higher accuracy regardless of the mode of operation. We performed vanilla gradient descent with a learning rate of 10^{-2}. (e) Best achieved test accuracy (dot) and fluctuations within the $+100$ and -100 epochs of the best attained accuracy (box plot). (f) Neuromorphic setup using the spin-diode effect: frequency and power of an incoming RF signal are used to encode the input data (frequency) and the weights (power), while, just as before, the accumulated voltages across a row serve as output. (g) The response of a single device to an RF signal at $B = 0$ (data from ref. [23]). We only show the response for signal powers $P/P_{\max} \in [0.4, 0.65]$ since outside of this regime, the response is relatively featureless. The frequency axis has been rescaled such that the measurement interval $[f_{\min}, f_{\max}]$ aligns with $[0, 1]$. (h) Training and test accuracy of the simulated neuromorphic chip based on the spin-diode effect.

vortex-MTJ platform, a bTMS mode and a spin-diode mode, both parameterized by measured, reproducible response maps (Supplementary Notes 1 and 2) rather than idealized transfer functions. In both modes, the trainable weights are physical drive parameters: the dc bias current in the bTMS mode and the RF power in the spin-diode mode. The non-volatile storage layer provides a persistent device-level tuning parameter [23] but is not trained in the present simulations, so storage-layer programming is not repeated during inference.

A. Neuromorphic computing based on the bTMS effect

First, we consider the bTMS effect and simulate the operation of a neuromorphic chip based on the measured device response to the laser power and bias current, Fig. 5 **a**. The devices are arranged in a crossbar-like configuration, Fig. 5 **b**, such that the incident laser powers across the jth column are set identical to the jth component of the input $x_j = P_{\ell,j}/P_{\max}$ for all rows ℓ with $P_{\max}$ the maximal input power considered. The bias currents can be chosen individually for each device and serve as trainable weights $W_{j,\ell} = I_{j,\ell}/I_{\max}$. The current is rescaled by the maximum bias current considered. The output voltages of each device are collected such that the sum of the voltages across one row can be measured as the accumulated output voltage, which serves as the network output of one neural network layer $y = V/V_{\max}$. The devices can be operated in a parallel or antiparallel configuration.

To investigate the performance of a neuromorphic chip based on this principle, we simulate the chip operation based on the measured bTMS response and test its performance on a standard classification task of hand-written digit recognition [56].

To train the simulated chip, we define a differentiable interpolation function $f(x_j, W_{j,\ell})$ in the Python library JAX which interpolates the output voltages of one device linearly between measurement data points as a function of input power (representing the input data x_j) and bias current (representing the weights $W_{j,\ell}$)

$$f_{j,\ell}(x_j, W_{j,\ell}) = \frac{V_{j,\ell}}{V_{\max}} \left(\frac{P_j}{P_{\max}}, \frac{I_{j,\ell}}{I_{\max}} \right). \tag{4}$$

The accumulated values $y_\ell = \sum_j f_{j,\ell}(x_j, W_{j,\ell})$ serve as the ℓth output. We show the interpolation functions for different device diameters and device operations (antiparallel vs. parallel) in Fig. 5 **c**.

For our simulations, we consider an array of 64×10 magnetic tunnel junctions representing a single neural network layer mapping from the pixel values of the input images to the output vector in which each vector entry represents one class with the maximal entry indicating the class. During training, we minimize the categorical cross-entropy loss function. We train the simulated chip by performing differentiation with JAX on the loss function. In the future, we envisage that the training would be performed directly on the chip with physics-based training methods [57] such as Equilibrium propagation [58] or a method recently proposed for nonlinear systems [59]. Such efficient physics-based training methods have the advantage that they allow us to perform the training directly in the hardware, enabling successful training even in the presence of device imperfections.

We train for $12,000$ epochs to ensure that the loss function has converged for all tested configurations. The classification accuracy on the test set during the training is shown in Fig. 5 **d**. We see that the smaller devices at 600 nm generally perform better than the larger devices at 800 nm. We attribute this to the stronger bias dependence of the small devices, which provides a wider range of effective weights. Furthermore, the maximal test accuracy is slightly higher for devices operated in a parallel configuration than in an antiparallel configuration. This may be due to the smaller training gradients obtained in the antiparallel configuration, such that the training may get stuck in local minima, although such problems could, in principle, be resolved through the use of optimizers such as Adam. The smaller training gradients also lead to a slower initial increase of the test accuracy. We show the best attained test accuracies in Fig. 5 **e** as well as the fluctuations over the 200 epochs around the best attained accuracy; because no separate validation set was used, the best accuracies are upper estimates. The best bTMS configuration reaches a test accuracy of 95.4%. Overall, the test accuracies are higher than in the previously investigated devices [31] and are now comparable to the accuracy of 95 % which we achieved by a single-layer digital artificial neural network of the same size with sigmoid activations. We attribute this improvement to the more pronounced bias dependence of the present devices. Hence, the bias dependence of the device response is a resource for neuromorphic computing.

B. Neuromorphic computing based on the spin-diode effect

Next, we consider the spin-diode effect for the purpose of neuromorphic computing by utilising the device's nonlinear response to an RF signal. Concretely, we encode the input data in the RF frequency while we encode the weights in the power, Fig. 5 **f**. As before, we consider a crossbar arrangement of the devices similar to Fig. 5 **b**. The accumulated voltages across one row determine one component of the output vector. This encoding has the advantage that, in contrast to the previous setup, which required bias currents to encode the weights, here, both input and weights are encoded in the RF signal, which implies that devices can potentially have an even smaller footprint since no individual bias lines are needed. Furthermore, changing the RF power has a lower latency than changing the bias currents, which can potentially result in a speed-up of an in-situ training process.

Again, we use a differentiable interpolation function based on the measurements to simulate the device response shown in Fig. 5 **g** for a single device and train the simulated neuromorphic chip on the image classification task. During training, we compute the gradients w.r.t. the signal power of each device. We initialise the powers in the range $P/P_{\max} \in [0.47, 0.57]$, the most structured part of the response, since flatter regions would result in small gradients, which we empirically found hinders and in some cases even prevents the training. We show the training and test accuracy of the neuromorphic system during the training in Fig. 5 **h** with a best attained test accuracy of 94.9%. This demonstrates that the spin-diode effect is another important resource for neuromorphic computing, with the advantage that spin-diode-based chips could offer a smaller spatial footprint and lower latency than bTMS-based devices. Supplying individually controlled RF signals to many devices, which would otherwise require complex multi-port RF hardware, is addressed in Sec. V.

C. Combining the bTMS and the spin-diode effect

Remarkably, both the bTMS effect and the spin-diode effect produce voltage changes of similar magnitude, so neither channel would dominate a combined response. Since the bTMS effect and the spin-diode effect are present in the same device, we propose combining them. A single device would then be subject to optical heating, a bias current, and an RF signal, such that the induced voltage depends nonlinearly on four parameters which can be reconfigured during device operation: the laser power, the bias current, the RF power, and the RF frequency. Hence, the device would be

able to implement a nonlinear function

$$g(x_1, x_2, W_1, W_2) = \frac{V}{V_{\max}} \left(\frac{P^{\text{laser}}}{P^{\text{laser}}_{\max}}, \frac{f - f_{\min}}{f_{\max} - f_{\min}}, \frac{I}{I_{\max}}, \frac{P^{\text{RF}}}{P^{\text{RF}}_{\max}} \right) \tag{5}$$

of two inputs, the laser power x_1 and the RF frequency x_2, with two weights, the bias current W_1 and the RF power W_2. To motivate the power of such an approach, we consider the Taylor expansion of g around a suitable operating point $(x_1^{(0)}, x_2^{(0)})$,

$$g \approx g_0 + c_1\,\delta x_1 + c_2\,\delta x_2 + b_{12}\,\delta x_1\,\delta x_2 + b_{11}\,\delta x_1^2 + b_{22}\,\delta x_2^2, \tag{6}$$

where $\delta x_i = x_i - x_i^{(0)}$ and all coefficients depend on W_1 and W_2. The cross-term $b_{12}\,\delta x_1\,\delta x_2$ multiplies the two inputs within a single device, so in a suitable regime this approach already enables quadratic processing that combines multiple inputs in one nanoscale element.

The physics of the junction provides the couplings that make b_{12} nonzero. Laser heating lowers the saturation magnetization and with it the gyrotropic frequency, which scales with the magnetization [60], and it reduces the tunnel magnetoresistance that sets the rectified amplitude; the spin-diode response to the RF frequency therefore depends on the laser power. The dc bias current, in turn, exerts a spin-transfer torque on the vortex and modifies its resonance [33]. Measuring the spin-diode spectrum at several laser powers, which yields b_{12} directly, is therefore a simple first experimental test of the combined mode.

Many modern machine learning operations rely on such nonlinear interactions between features (inputs), including the attention mechanism, recurrent neural networks, and graph neural networks [61–63]. Conventional in-memory computing arrays multiply inputs by stored weights but cannot form products of two inputs directly, and on digital hardware such operations add substantially to the computational cost. Implementing them within a single nonlinear device, or across a crossbar array, therefore offers a route to their acceleration. An N-device row of a combined bTMS–spin-diode array, in which each device processes two inputs simultaneously, performs the equivalent of $3N - 1$ elementary operations ($2N$ multiplications and $N - 1$ summations); together with the nanoscale footprint of MTJs, this can enable a high intrinsic compute density, which we estimate in the next subsection together with the energy per operation.

D. Energy per operation and comparison with neuromorphic hardware

We estimate the active energy cost of an inference operation by integrating the applied drive power over the relevant operation time, $E_{\text{op}} = P_{\text{drive}}\tau_{\text{op}}$. The non-volatile programming of the storage layer is treated separately, since it corresponds to an infrequent weight-update step rather than a cost paid during every inference cycle. In the spin-diode mode, the active drive is the applied RF excitation. For the experimentally used powers of -10 to -5 dBm, corresponding to 0.10–0.32 mW, and the damping time of the gyrotropic mode as the operation time, $\tau_{\text{op}} \approx 1/(\pi\Delta f) \approx 0.03$–$0.3$ μs (Sec. II), this gives an RF drive energy of $E_{\text{op}} \approx$ 3–100 pJ per device evaluation. Practical readout energy will depend on the required integration time, RF coupling, amplification, and peripheral circuitry. If the readout is integrated for longer to improve signal-to-noise ratio, this value scales approximately linearly with the integration time. The additional dc-bias dissipation is small on this scale: using $RA \approx 10\ \Omega\,\mu\text{m}^2$, a 600 nm junction has $R \approx 35\ \Omega$, so a bias current of $I = 0.5$ mA dissipates only $I^2R \approx 9\ \mu$W.

The bTMS mode is presently limited by the free-space optical heating configuration rather than by the intrinsic MTJ element. With on-state laser powers $P_{\text{laser}} =$ 15–67 mW, a 1 kHz optical modulation/readout cadence and a 50% duty cycle, the laser is on for 0.5 ms of each period, so the corresponding active optical energy is 7.5–33.5 μJ per modulation period. This number should therefore be understood as the cost of the proof-of-principle optothermal measurement configuration, not as an optimized device limit. As discussed in Sec. V, integrated VCSEL/microlens delivery would concentrate the optical power at the nanopillar; however, the energy per operation for this configuration requires a transient thermal analysis of the complete device stack and is not projected here. The storage-layer programming pulse is again a separate cost: a 0.9 V, 1 ms Joule-heating pulse gives an estimated write energy of order $\sim$20 μJ, using the nominal junction resistance during the pulse. All values reported here are device-level active-drive estimates and do not include laser wall-plug efficiency, RF-source losses, impedance-matching networks, ADC/DAC conversion, or peripheral circuitry.

Table I places these estimates in the context of representative spintronic, analog in-memory, and digital neuromorphic hardware. Such a comparison must be made carefully because the reported metrics are not uniform: different works quote per-MAC inference energy, synaptic-update energy, weight-write energy, per-spike energy, or simulated network-level projections. Where possible, we convert reported energy efficiencies to an approximate per-MAC value using 1 MAC = 2 operations, and we label each number as measured [R], derived [D], or simulated/projected [S]. The

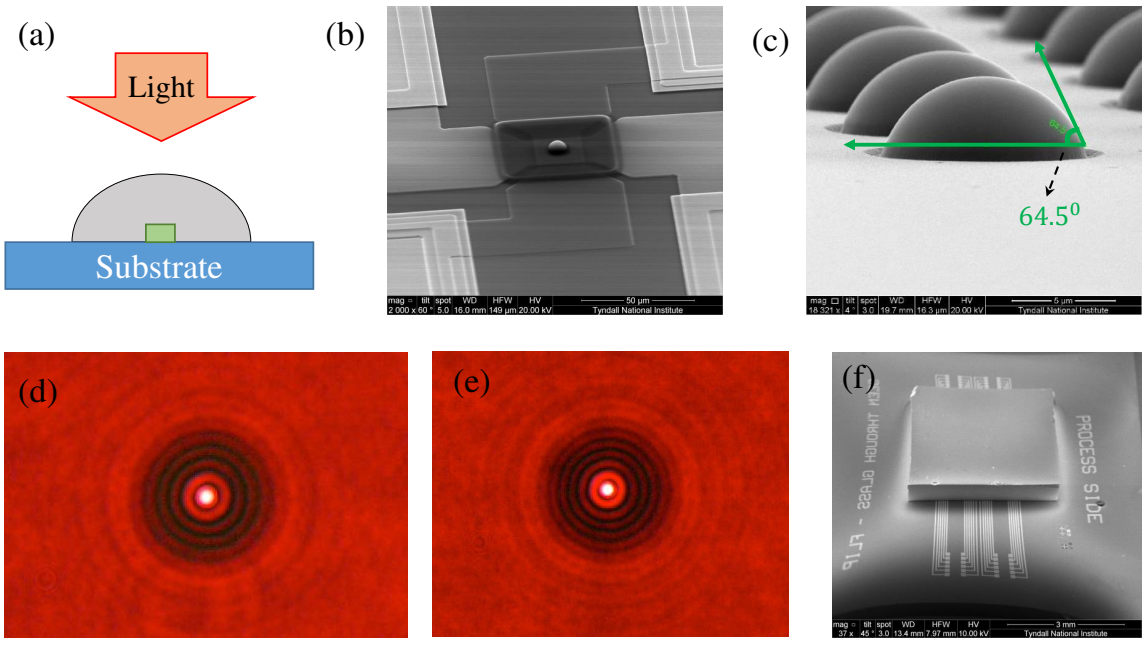


FIG. 6. **Experimental route to integrated optical addressing of the MTJ array.** (a) Schematic of the addressing geometry: light focused by a hemispheric microlens onto a nanopillar on a substrate. (b) SEM of a PMGI microlens formed over a nanopillar device structure. (c) SEM of an array of PMGI microlenses; the measured lens contact angle is 64.5°. (d) Focused 633 nm light from an 8.5 μm-diameter microlens (focal spot ∼960 nm). (e) Focused 633 nm light from a 6.5 μm-diameter microlens (focal spot ∼870 nm). (f) SEM of the fabricated VCSEL array flip-chip mounted on a patterned glass substrate.

spin-diode drive energy derived above is not directly equivalent to a measured system-level energy per MAC, as it excludes readout integration, RF coupling losses, conversion, and peripheral circuitry; direct numerical comparison with full-system values such as those reported for PCM accelerators (≈0.2–0.8 pJ/MAC [64, 65]) or digital neuromorphic processors, including Loihi (23.6 pJ/SynOp [66]), TrueNorth (26 pJ/event [67]), and ODIN (12.7 pJ/SOP [68]), should therefore be made with caution. It remains higher than the measured 508 fJ/operation reported for domain-wall MTJ synapse–neuron circuits [69] and higher than the fJ-scale projections for aggressively scaled 20 nm RF-MTJ networks [35]. In contrast, the present bTMS mode should be viewed primarily as a non-contact optothermal nonlinear readout: it provides a strong intrinsic cubic response and optical input channel, but its current free-space implementation is not yet energy optimized. To our knowledge, no established tunnel-magneto-Seebeck neuromorphic energy benchmark exists for a direct comparison.

In addition to energy, the MTJ geometry offers a route to high intrinsic compute density. For the combined mode, with $3N-1$ elementary operations per N-device row (Sec. IV C), and assuming a scaled ∼1 μm^2 device footprint and a conservative 1 MHz device-evaluation rate, the hypothetical combined bTMS–spin-diode mode gives a projected device-array density of $\sim 3\times10^{12}$ operations s^{-1} mm^{-2}, or ∼3 TOPS mm^{-2}. At the present fabricated footprint of ∼25 μm^2 per device, the corresponding value decreases to ∼0.12 TOPS mm^{-2}, while the present 1 kHz free-space bTMS implementation gives a much lower practical throughput. This projected combined-mode density is in the same order-of-magnitude range as measured full-core analog in-memory accelerators, such as HERMES-Core (1.59 TOPS mm^{-2} [64]) and the IBM 64-core PCM inference chip (1.55 TOPS mm^{-2} in single-phase operation and ∼0.39 TOPS mm^{-2} in four-phase operation [65]). This comparison should not be interpreted as a direct ranking: our value is a projected device-array estimate at analog precision and excludes optical-addressing pitch, thermal guard spacing, routing and peripheral overhead, whereas the comparator values are measured full-core densities at 8-bit integer precision. Rather, the comparison shows that, after scaling, vortex-MTJ arrays could enter the same compute-density regime as leading non-volatile analog in-memory-compute platforms while offering distinct RF and optothermal nonlinearities.

TABLE I. Energy per operation and compute density of the present platform compared with representative spintronic, analog in-memory, and digital neuromorphic hardware. Because the reported metrics differ across platforms, each entry is listed according to its native operation and converted to a per-MAC basis where possible using 1 MAC = 2 operations. Flags: [R] measured, [D] derived from reported drive power, operating frequency, or energy efficiency, and [S] simulated/projected; n.r. = not reported. "Drive incl." indicates whether the optical/RF/bias drive is included fully (Y), partially (P), or not included (N). Values for the present work are device-level active-drive estimates and do not include wall-plug losses or peripheral circuitry. Comparator compute densities are measured full-core values at 8-bit integer precision where specified.

Platform	Operation/metric	Energy per operation (flag)	Compute density	Drive incl.
This work — vortex MTJ				
Spin-diode mode	RF-driven device evaluation	≈3–100 pJ per evaluation, from $P_{\mathrm{RF}}\tau_{\mathrm{op}}$ with $\tau_{\mathrm{op}} \approx 1/(\pi\Delta f)$ for linewidths of 1–10 MHz [D]	–	P
bTMS mode (free-space)	optical readout	7.5–33.5 μJ per 1-ms modulation period in the present setup [D]	–	Y
bTMS mode (integrated, projected)	optical readout	not projected; requires transient thermal analysis [S]	∼3 TOPS/mm^2 (combined-mode projection)	Y
Weight programming	storage-layer write	∼20 μJ/write, one-time non-volatile update [D]	–	Y
Spintronic neuromorphic devices				
Vortex STNO reservoir [16]	oscillator reservoir	n.r. (context)	–	N
Coupled STNOs [17]	coupled-oscillator classification	n.r. (context)	–	N
Weighted STNO [12]	MRAM-synapse write	30 pJ/write for a 1 ns pulse (350 mV at the field line) [R]	–	P
2D SHNO array [11]	oscillator synchronization	n.r. (context)	–	N
RF spin-diode synapse [34]	RF multiply–accumulate concept	n.r. (context)	–	N
RF MTJ network [35]	RF network at 20 nm	10 fJ/syn, 100 fJ/neu [S]	–	Y
DW-MTJ synapse [70]	weight-modulation event	≤16 pJ/update [R]; ∼fJ scaled [S]	–	P
DW-MTJ synapse + neuron [69]	all-spin synapse/neuron operation	508 fJ/op, with 36 fJ/pulse for sigmoid generation [R]	–	P
Skyrmion synapse [71]	synaptic update	n.r. (device paper)	–	–
Analog in-memory compute (CMOS)				
HERMES-Core PCM [64]	analog MAC, 8-bit, 14 nm	≈190 fJ/MAC, derived from 10.5 TOPS/W [D]	1.59 TOPS/mm^2 [R]	Y
IBM 64-core PCM [65]	analog MAC, 8-bit	≈205 fJ/MAC in single-phase operation; ≈806 fJ/MAC in four-phase operation [D]	1.55 / 0.39 TOPS/mm^2 [R]	Y
Digital neuromorphic processors (CMOS)				
Loihi [66]	synaptic operation	23.6 pJ/SynOp [R]	–	Y
TrueNorth [67]	synaptic event	26 pJ/event [R]	–	Y
ODIN [68]	synaptic operation, 28 nm	12.7 pJ/SOP [R]	–	Y

V. CONTROL PRECISION AND ROUTES TO INTEGRATED OPTICAL AND RF ADDRESSING

A natural concern for any analog neuromorphic platform is whether finite control precision in the laser power, dc bias current, and RF signal limits practical operation. Two considerations indicate that this is not a fundamental obstacle. First, the scheme inherits the intrinsic tolerance of analog in-memory and physical neural networks to imperfect control: state-of-the-art non-volatile analog accelerators reach software-comparable accuracy with only 3–4 effective bits of analog precision [64, 72], and the physics-based on-chip training methods envisaged for this platform [57–59]

are designed to absorb device variation and noise during learning. Exact open-loop setting of every physical input is therefore not required for reliable inference. Second, the experimentally relevant control precision is already compatible with the device requirements. Closed-loop optical-power stabilisation using a monitor photodiode can reach the 0.1–1% level, corresponding to $\lesssim$1 K fluctuations on the $\sim$100 K operating temperature rise obtained from finite-element thermal modelling (Supplementary Note 7). Integrated current sources can supply the dc-bias weights at the few-bit resolution already sufficient for high-accuracy analog arrays [64, 72]. Likewise, standard RF sources provide frequency precision far below the megahertz-scale gyrotropic linewidth and the $\sim$15 MHz non-volatile tuning range that define the spin-diode operating window [23], while RF-power errors of order $\lesssim$0.5 dB are small compared with the power range over which the rectified spin-diode weight varies. Residual imprecision can therefore be treated as part of the analog device variation and compensated during training or calibration, rather than representing a fundamental limitation.

Dense deployment of the bTMS mode additionally requires delivering focused light to individual nanopillars without thermal crosstalk. An analytical Green's-function estimate for a Gaussian surface heat source on a semi-infinite substrate [73] suggests a few-percent crosstalk length of several tens of micrometres for the present 7 μm spot; this length scale can be reduced toward the micrometre range by diffraction-limited or integrated microlens/VCSEL delivery, consistent with finite-element studies of laser-heated CoFeB/MgO junctions that reproduce measured thermovoltages and temperature-gradient decay on comparable scales [74]. Junctions that intentionally share the same optical input can therefore be heated collectively, whereas neighbouring input columns carrying different signals require thermal guard spacing. Because this estimate omits the full multilayer stack, contacts, absorption profile and interface resistances, it gives a crosstalk length scale rather than a full device-scale thermal map, and a full neighbouring-device thermal simulation remains necessary to determine the practical crosstalk-limited array pitch. As a concrete route, a two-dimensional array of vertical-cavity surface-emitting lasers (VCSELs) can be flip-chip mounted above the MTJ array, with each beam focused by an integrated microlens onto the underlying nanopillar [Fig. 6(a)]. This concentrates the optical intensity at the nanopillar, relaxes alignment tolerances, and—through monitor-photodiode feedback—can provide the per-emitter power stabilisation discussed above. Finite-element thermal simulations indicate that $\sim$2 mW of focused VCSEL power is sufficient to generate the $\sim$100 K temperature rise required for bTMS operation when the beam is concentrated close to the optical wavelength (Supplementary Note 7). As a simple geometric intensity estimate, 1 mW focused into a $\sim$1 μm spot gives an optical intensity comparable to $\sim$50 mW in the present free-space 7 μm spot, although the actual temperature rise also depends on lateral heat spreading, multilayer absorption, and interface thermal resistances. We have experimentally realised the enabling integration components (Fig. 6): microlenses formed by controlled reflow of polydimethylglutarimide (PMGI) resist [75]—transparent across the visible and near-infrared and compatible with SAC-solder flip-chip processing—were obtained with a well-defined profile [contact angle 64.5°; Fig. 6(c)] and focus 633 nm light, close to the 638 nm operating wavelength, to submicron spots [$\sim$960 and $\sim$870 nm for 8.5 and 6.5 μm-diameter lenses; Fig. 6(d,e)]. Such a microlens can be formed directly over a nanopillar device [Fig. 6(b)], and a fabricated VCSEL array has been flip-chip mounted with a $\sim$126 μm emitter pitch onto a patterned glass carrier [Fig. 6(f)]; this pitch demonstrates the integration process rather than the target array pitch. Microlens arrays have recently been designed for bolometers based on stochastic magnetic tunnel junctions [76], but to our knowledge, neither a microlens formed directly on a magnetic tunnel junction nor a laser array for addressing such junctions has been reported before. Resonant photonic structures, such as one-dimensional photonic-crystal cavities and aperiodic (magneto-)photonic multilayers, which strongly concentrate optical fields [77–79], could further reduce the optical power needed per junction. Together with the thermal-crosstalk scaling discussed above, these results establish a practical route towards integrated, individually addressable, and power-stabilised optical excitation.

In the spin-diode mode, scalable operation does not require a separate RF generator for each junction. Each vortex MTJ acts as a local RF-to-dc rectifier: an applied AC signal excites the gyrotropic mode, and the oscillating tunnel resistance converts this excitation into a measurable dc voltage. The gyrotropic frequency is set by the nanopillar geometry and can be shifted non-volatilely over a $\sim$15 MHz range by the storage-layer state [23, 35]. Neighbouring devices can therefore be assigned distinct frequency channels and addressed through a shared frequency-multiplexed RF line, so the requirement is not one generator per device but controlled channel spacing and readout. The storage layer provides a second, complementary route that does not require drive multiplexing: a fixed AC excitation can be passed sequentially through several MTJs, with each junction producing a different rectified dc voltage according to its individually programmed magnetic state. For example, at 135 MHz and -5 dBm, storage-layer reconfiguration tunes the rectified output almost linearly from $+6$ to -3 mV [23]. Thus, the analog weight can be supplied directly by the persistent magnetic configuration. For the present devices, the number of reliably distinguishable series-addressed junctions is mainly limited by the reproducibility of the storage-layer reconfiguration, including scatter from the modest exchange bias and defect-related pinning, giving, by our estimate, roughly 15–20 distinguishable contributions; stronger exchange bias and improved pinning control should extend this number to several tens. Sneak-path currents in passive crossbars are circuit-level issues rather than fundamental device limitations and can be mitigated by CMOS integration with per-device access transistors, while RF distribution additionally requires impedance-matched lines. The MTJ process is CMOS-compatible and has already been implemented on full CMOS wafers in related demonstrators [55].

In such an architecture, and because each junction acts as a local RF detector and rectifier, an integrated RF source shared across the array reduces to a dc current source, a spintronic oscillator, and an RF amplifier, rather than a per-device vector network analyser.

VI. CONCLUSION

We have established a storage-layer-enabled vortex MTJ as a multifunctional neuromorphic device that unifies, within a single nanopillar architecture, three capabilities hitherto treated in isolation: non-volatile magnetic programmability, laser-driven spin-caloritronic operation and nonlinear vortex-dynamical rectification. Building on the non-volatile, continuous tuning of the gyrotropic resonance by the integrated storage layer [23], we extend this platform to laser-induced thermal gradients and resolve both the linear TMS and the bias-enhanced bTMS regimes. In the TMS regime, the thermovoltage switches with the magnetic state and scales linearly with laser power, reproducibly across nine junctions; in the bTMS regime, a pronounced cubic bias dependence makes the bias current a compact, programmable nonlinear weight for the optical input.

Using the measured responses, simulated crossbar networks reach 95.4% (bTMS) and 94.9% (spin-diode) accuracy in handwritten-digit classification, comparable to a digital single-layer network, and smaller junctions perform better, identifying the bias dependence of the response as a device-level design parameter. Because both channels coexist in the same junction, simultaneous optical, dc and RF excitation could generate cross-terms between optical and RF inputs within a single nanoscale element, an operation that conventional in-memory computing arrays cannot perform directly. Microlenses with sub-micrometre focal spots, including, to our knowledge, the first formed directly on a magnetic tunnel junction, and a flip-chip-mounted VCSEL array provide the components for on-chip optical addressing. A small hardware crossbar, a device-scale thermal-crosstalk map and a measurement of the optical–RF cross-term are the next steps towards a complete system-level demonstration. Together, these results establish vortex MTJs as a multifunctional nanoscale platform in which programmable magnetism, spin caloritronics and gyrotropic dynamics converge to implement nonlinear primitives for next-generation neuromorphic hardware.

VII. METHODS

A. Device structure and fabrication

The devices were fabricated at INL in the same run as those of ref. [23]. Magnetic tunnel junction stacks were deposited by magnetron sputtering (Singulus TIMARIS Multi-Target-Module) onto 200-mm thermally oxidised silicon wafers [Si/SiO_2(200 nm)]. The stack, from bottom to top, was [Ta(5)/CuN(25)]$_6$/Ta(5)/Ru(5)/$Ir_{20}Mn_{80}$(15)/$Co_{70}Fe_{30}$(2)/Ru(0.825)/$Co_{40}Fe_{40}B_{20}$(2.6)/MgO/$Co_{40}Fe_{40}B_{20}$(2)/Ta(0.21)/NiFe(7)/Cu(10)/NiFe(6)/$Ir_{20}Mn_{80}$(6)/Ta(10)/Ru(7)/TiWN(15)/AlSiCu(200)/TiWN(15), with thicknesses in nanometres. In this stack, $Ir_{20}Mn_{80}$(15) is AFM1, $Co_{70}Fe_{30}$(2)/Ru(0.825)/$Co_{40}Fe_{40}B_{20}$(2.6) is the SAF reference layer, $Co_{40}Fe_{40}B_{20}$(2)/Ta(0.21)/NiFe(7) is the vortex free layer, Cu(10) is the non-magnetic spacer and NiFe(6)/$Ir_{20}Mn_{80}$(6) is the storage layer (AFM2). The MgO thickness was chosen to give a resistance–area product of about 10 $\Omega\,\mu m^2$ [23]. The sublayers beneath AFM1 were optimized to minimise surface roughness and serve as the bottom electrical contact. Nanopillars with diameters of 600, 800 and 1000 nm were patterned by electron-beam lithography and ion-beam milling, embedded in SiO_2 for electrical isolation, and then contacted from the top. The devices were annealed at 330 °C for 2 h in an in-plane field of 1 T to set the exchange bias at both ferromagnet/antiferromagnet interfaces. The blocking temperatures of AFM1 (about 230 °C) and AFM2 (about 180 °C) were determined on continuous films by thermal vibrating-sample magnetometry; they are approximate, as patterning may lower them. The storage layer is programmed as described in ref. [23]: a voltage pulse of 0.9 V and 1 ms Joule-heats the junction above the blocking temperature of AFM2 but below that of AFM1, and cooling in a reconfiguration field B_{REC} of up to ±35 mT freezes the new storage-layer configuration. The stray field of the storage layer acting on the free layer (Fig. 1d) was obtained from micromagnetic simulations with MuMax3 [80], as described in ref. [23].

B. TMS and bTMS measurement protocol

Optothermal measurements were performed at the University of Greifswald. Junctions of different diameter on the same chip were characterized one at a time: in each measurement, one junction was contacted electrically and heated by a 638-nm diode laser, square-wave modulated at 1 kHz with a 50% duty cycle and focused to a spot of about 7 μm diameter, with on-state laser powers at the sample of 15–67 mW. Because only one junction is heated at a time, thermal

crosstalk between devices does not affect the reported data. The thermal diffusion time over the heated region (about 1 μs for 10 μm in silicon) is much shorter than the 0.5-ms half-period, so the temperature profile is quasi-steady within each half-period. TMS measurements were performed in open circuit, without bias current; for bTMS measurements, a dc bias current I was applied through the junction during laser heating. In both cases, the first-harmonic voltage at the modulation frequency was detected with a lock-in amplifier referenced to the laser modulation and is reported as the laser on/off difference $\Delta V_{\mathrm{AC}} = V_{\mathrm{AC,on}} - V_{\mathrm{AC,off}}$; under bias, a parallel dc channel recorded the time-averaged voltage V_{DC}. For each laser power and, in the bTMS measurements, each bias current, the in-plane magnetic field was swept through the parallel and antiparallel states, and the P- and AP-state voltages were read off at $B_{\parallel} = \pm 30$ mT; high-resolution sweeps used 0.25-mT steps. Three observations support a thermoelectric origin of the zero-bias signal: it switches between two levels at the magnetic switching fields (Fig. 2a–c), it scales linearly with laser power (Fig. 2d–f), and its phase is fixed relative to the optical reference. Under bias, V_{DC} vanishes at $I = 0$ and reverses sign with the bias current, as expected for a coupled thermal–electrical origin rather than an instrumental artefact. The bias dependences in Fig. 4 were fitted with cubic polynomials $V(I) = \sum_{n=0}^{3} a_n I^n$. Zero-bias measurements were performed on nine junctions, three nominally identical devices per diameter, and laser-power sweeps on two 800-nm junctions were repeated over several months (Supplementary Note 1). The bias-enhanced response was compared run to run on one 800-nm junction and device to device on two 800-nm and four 600-nm junctions (Supplementary Note 2).

ACKNOWLEDGMENTS

This project was supported by funding from the European Union's Horizon 2020 research and innovation programme under grant agreement No. 899559 (SpinAge).

DATA AVAILABILITY

Data are available from the corresponding authors upon reasonable request. The spin-diode data were reported in ref. [23].

CODE AVAILABILITY

The code used for the neural-network simulations is available from the corresponding authors upon reasonable request.

COMPETING INTERESTS

The authors declare no competing interests.

[1] M. Davies, Benchmarks for progress in neuromorphic computing, Nat. Mach. Intell. **1**, 386 (2019).
[2] D. Marković, A. Mizrahi, D. Querlioz, and J. Grollier, Physics for neuromorphic computing, Nat. Rev. Phys. **2**, 499 (2020).
[3] R. W. Keyes, Physical limits in semiconductor electronics, Science **195**, 1230 (1977).
[4] J. B. Aimone, P. Date, G. A. Fonseca-Guerra, K. E. Hamilton, K. Henke, B. Kay, G. T. Kenyon, S. R. Kulkarni, S. M. Mniszewski, M. Parsa, S. R. Risbud, C. D. Schuman, W. Severa, and J. D. Smith, A review of non-cognitive applications for neuromorphic computing, Neuromorph. Comput. Eng. **2**, 032003 (2022).
[5] C. H. Marrows, J. Barker, T. A. Moore, and T. Moorsom, Neuromorphic computing with spintronics, npj Spintronics **2**, 12 (2024).
[6] J. Grollier, D. Querlioz, K. Y. Camsari, K. Everschor-Sitte, S. Fukami, and M. D. Stiles, Neuromorphic spintronics, Nat. Electron. **3**, 360 (2020).
[7] J. Zhou and J. Chen, Prospect of spintronics in neuromorphic computing, Adv. Electron. Mater. **7**, 2100465 (2021).
[8] A. F. Vincent, J. Larroque, N. Locatelli, N. Ben Romdhane, O. Bichler, C. Gamrat, W. S. Zhao, J.-O. Klein, S. Galdin-Retailleau, and D. Querlioz, Spin-transfer torque magnetic memory as a stochastic memristive synapse for neuromorphic systems, IEEE Trans. Biomed. Circuits Syst. **9**, 166 (2015).

[9] A. Kurenkov, S. DuttaGupta, C. Zhang, S. Fukami, Y. Horio, and H. Ohno, Artificial neuron and synapse realized in an antiferromagnet/ferromagnet heterostructure using dynamics of spin–orbit torque switching, Adv. Mater. **31**, 1900636 (2019).

[10] U. Shashank, A. Kumar, T. S. Parvini, H. Heyen, L. Zeng, A. B. Yankovich, J.-G. Choi, M. Rajabali, E. Olsson, M. Münzenberg, and J. Åkerman, Bulk spin–orbit torque-driven spin Hall nano-oscillators using PtBi alloys with engineered crystallinity, ACS Appl. Mater. Interfaces **18**, 39941 (2026).

[11] M. Zahedinejad, A. A. Awad, S. Muralidhar, R. Khymyn, H. Fulara, H. Mazraati, M. Dvornik, and J. Åkerman, Two-dimensional mutually synchronized spin Hall nano-oscillator arrays for neuromorphic computing, Nat. Nanotechnol. **15**, 47 (2020).

[12] T. Böhnert, Y. Rezaeiyan, M. S. Claro, L. Benetti, A. S. Jenkins, H. Farkhani, F. Moradi, and R. Ferreira, Weighted spin torque nano-oscillator system for neuromorphic computing, Commun. Eng. **2**, 65 (2023).

[13] M. Kammerer, M. Weigand, M. Curcic, M. Noske, M. Sproll, A. Vansteenkiste, B. Van Waeyenberge, H. Stoll, G. Woltersdorf, C. H. Back, and G. Schütz, Magnetic vortex core reversal by excitation of spin waves, Nat. Commun. **2**, 279 (2011).

[14] A. S. Jenkins, L. San Emeterio Alvarez, S. Memshawy, P. Bortolotti, V. Cros, P. P. Freitas, and R. Ferreira, Electrical characterisation of higher order spin wave modes in vortex-based magnetic tunnel junctions, Commun. Phys. **4**, 107 (2021).

[15] D. Suess, A. Bachleitner-Hofmann, A. Satz, H. Weitensfelder, C. Vogler, F. Bruckner, C. Abert, K. Prügl, J. Zimmer, C. Huber, S. Luber, W. Raberg, T. Schrefl, and H. Brückl, Topologically protected vortex structures for low-noise magnetic sensors with high linear range, Nat. Electron. **1**, 362 (2018).

[16] J. Torrejon, M. Riou, F. Abreu Araujo, S. Tsunegi, G. Khalsa, D. Querlioz, P. Bortolotti, V. Cros, K. Yakushiji, A. Fukushima, H. Kubota, S. Yuasa, M. D. Stiles, and J. Grollier, Neuromorphic computing with nanoscale spintronic oscillators, Nature **547**, 428 (2017).

[17] M. Romera, P. Talatchian, S. Tsunegi, F. Abreu Araujo, V. Cros, P. Bortolotti, J. Trastoy, K. Yakushiji, A. Fukushima, H. Kubota, S. Yuasa, M. Ernoult, D. Vodenicarevic, T. Hirtzlin, N. Locatelli, D. Querlioz, and J. Grollier, Vowel recognition with four coupled spin-torque nano-oscillators, Nature **563**, 230 (2018).

[18] Y. Imai, K. Nakajima, S. Tsunegi, and T. Taniguchi, Input-driven chaotic dynamics in vortex spin-torque oscillator, Sci. Rep. **12**, 21651 (2022).

[19] S. Tsunegi, T. Taniguchi, K. Nakajima, S. Miwa, K. Yakushiji, A. Fukushima, S. Yuasa, and H. Kubota, Physical reservoir computing based on spin torque oscillator with forced synchronization, Appl. Phys. Lett. **114**, 164101 (2019).

[20] D. Marković, N. Leroux, M. Riou, F. Abreu Araujo, J. Torrejon, D. Querlioz, A. Fukushima, S. Yuasa, J. Trastoy, P. Bortolotti, and J. Grollier, Reservoir computing with the frequency, phase, and amplitude of spin-torque nano-oscillators, Appl. Phys. Lett. **114**, 012409 (2019).

[21] M. Riou, J. Torrejon, B. Garitaine, F. Abreu Araujo, P. Bortolotti, V. Cros, S. Tsunegi, K. Yakushiji, A. Fukushima, H. Kubota, S. Yuasa, D. Querlioz, M. D. Stiles, and J. Grollier, Temporal pattern recognition with delayed-feedback spin-torque nano-oscillators, Phys. Rev. Appl. **12**, 024049 (2019).

[22] L. Martins, A. S. Jenkins, L. San Emeterio Alvarez, J. Borme, T. Böhnert, J. Ventura, P. P. Freitas, and R. Ferreira, Non-volatile artificial synapse based on a vortex nano-oscillator, Sci. Rep. **11**, 16094 (2021).

[23] M. Stebliy, A. S. Jenkins, L. Benetti, E. Paz, and R. Ferreira, Non-volatile analog control and reconfiguration of a vortex nano-oscillator frequency, Adv. Funct. Mater. **34**, 2405776 (2024).

[24] G. E. W. Bauer, E. Saitoh, and B. J. van Wees, Spin caloritronics, Nat. Mater. **11**, 391 (2012).

[25] K. Uchida, S. Takahashi, K. Harii, J. Ieda, W. Koshibae, K. Ando, S. Maekawa, and E. Saitoh, Observation of the spin Seebeck effect, Nature **455**, 778 (2008).

[26] T. Kuschel, M. Czerner, J. Walowski, A. Thomas, H. W. Schumacher, G. Reiss, C. Heiliger, and M. Münzenberg, Tunnel magneto-Seebeck effect, J. Phys. D: Appl. Phys. **52**, 133001 (2019).

[27] M. Walter, J. Walowski, V. Zbarsky, M. Münzenberg, M. Schäfers, D. Ebke, G. Reiss, A. Thomas, P. Peretzki, M. Seibt, J. S. Moodera, M. Czerner, M. Bachmann, and C. Heiliger, Seebeck effect in magnetic tunnel junctions, Nat. Mater. **10**, 742 (2011).

[28] N. Liebing, S. Serrano-Guisan, K. Rott, G. Reiss, J. Langer, B. Ocker, and H. W. Schumacher, Tunneling magnetothermopower in magnetic tunnel junction nanopillars, Phys. Rev. Lett. **107**, 177201 (2011).

[29] A. Boehnke, U. Martens, C. Sterwerf, A. Niesen, T. Huebner, M. von der Ehe, M. Meinert, T. Kuschel, A. Thomas, C. Heiliger, M. Münzenberg, and G. Reiss, Large magneto-Seebeck effect in magnetic tunnel junctions with half-metallic Heusler electrodes, Nat. Commun. **8**, 1626 (2017).

[30] A. Boehnke, M. Milnikel, M. von der Ehe, C. Franz, V. Zbarsky, M. Czerner, K. Rott, A. Thomas, C. Heiliger, G. Reiss, and M. Münzenberg, On/off switching of bit readout in bias-enhanced tunnel magneto-Seebeck effect, Sci. Rep. **5**, 8945 (2015).

[31] F. Oberbauer, T. J. Winkel, T. Böhnert, C. C. Wanjura, M. S. Claro, L. Benetti, I. Çaha, F. L. Deepak, F. Moradi, R. Ferreira, M. Münzenberg, and T. S. Parvini, Magnetic tunnel junctions driven by hybrid optical-electrical signals as a flexible neuromorphic computing platform, Commun. Phys. **8**, 329 (2025).

[32] A. A. Tulapurkar, Y. Suzuki, A. Fukushima, H. Kubota, H. Maehara, K. Tsunekawa, D. D. Djayaprawira, N. Watanabe, and S. Yuasa, Spin-torque diode effect in magnetic tunnel junctions, Nature **438**, 339 (2005).

[33] A. S. Jenkins, R. Lebrun, E. Grimaldi, S. Tsunegi, P. Bortolotti, H. Kubota, K. Yakushiji, A. Fukushima, G. de Loubens, O. Klein, S. Yuasa, and V. Cros, Spin-torque resonant expulsion of the vortex core for an efficient radiofrequency detection scheme, Nat. Nanotechnol. **11**, 360 (2016).

[34] N. Leroux, A. Mizrahi, D. Marković, D. Sanz-Hernández, J. Trastoy, P. Bortolotti, L. Martins, A. Jenkins, R. Ferreira, and J. Grollier, Hardware realization of the multiply and accumulate operation on radio-frequency signals with magnetic tunnel junctions, Neuromorph. Comput. Eng. **1**, 011001 (2021).

[35] A. Ross, N. Leroux, A. De Riz, D. Marković, D. Sanz-Hernández, J. Trastoy, P. Bortolotti, D. Querlioz, L. Martins, L. Benetti, M. S. Claro, P. Anacleto, A. Schulman, T. Taris, J.-B. Begueret, S. Saïghi, A. S. Jenkins, R. Ferreira, A. F. Vincent, F. A. Mizrahi, and J. Grollier, Multilayer spintronic neural networks with radiofrequency connections, Nat. Nanotechnol. **18**, 1273 (2023).

[36] A. Kirilyuk, A. V. Kimel, and T. Rasing, Ultrafast optical manipulation of magnetic order, Rev. Mod. Phys. **82**, 2731 (2010).

[37] T. J. Winkel, T. S. Parvini, F.-F. Stiewe, J. Walowski, F. Moradi, and M. Münzenberg, Comparative analysis of THz signal emission from bilayer heterostructures: Wideband and high-frequency THz signal advantage of PtBi-based emitter, Appl. Phys. Lett. **124**, 012408 (2024).

[38] H. Su, H. Kwon, F. Xue, N. Sato, U. Bhat, W. Tsai, M. Bosman, M. Asheghi, K. E. Goodson, E. Pop, and S. X. Wang, Thermal characterization of ultrathin MgO tunnel barriers, Nano Lett. **24**, 14567 (2024).

[39] H. Jang, L. Marnitz, T. Huebner, J. Kimling, T. Kuschel, and D. G. Cahill, Thermal conductivity of oxide tunnel barriers in magnetic tunnel junctions measured by ultrafast thermoreflectance and magneto-optic Kerr effect thermometry, Phys. Rev. Appl. **13**, 024007 (2020).

[40] J. M. Teixeira, J. D. Costa, J. Ventura, M. P. Fernandez-Garcia, J. Azevedo, J. P. Araujo, J. B. Sousa, P. Wisniowski, S. Cardoso, and P. P. Freitas, Giant intrinsic thermomagnetic effects in thin MgO magnetic tunnel junctions, Appl. Phys. Lett. **102**, 212413 (2013).

[41] M. Czerner, M. Bachmann, and C. Heiliger, Spin caloritronics in magnetic tunnel junctions: Ab initio studies, Phys. Rev. B **83**, 132405 (2011).

[42] L. Gravier, S. Serrano-Guisan, F. Reuse, and J.-P. Ansermet, Thermodynamic description of heat and spin transport in magnetic nanostructures, Phys. Rev. B **73**, 024419 (2006).

[43] R. Schmidt, F. Wilken, T. S. Nunner, and P. W. Brouwer, Boltzmann approach to the longitudinal spin Seebeck effect, Phys. Rev. B **98**, 134421 (2018).

[44] L. Onsager, Reciprocal relations in irreversible processes. I., Phys. Rev. **37**, 405 (1931).

[45] L. Onsager, Reciprocal relations in irreversible processes. II., Phys. Rev. **38**, 2265 (1931).

[46] N. Jha, A. Pariyar, T. S. Parvini, C. Denker, P. K. Vardhanapu, G. Vijaykumar, A. Ahrens, T. Meyer, M. Seibt, N. Atodiresei, J. S. Moodera, S. K. Mandal, and M. Münzenberg, Interface-assisted room-temperature magnetoresistance in Cu-phenalenyl-based magnetic tunnel junctions, ACS Appl. Electron. Mater. **5**, 1471 (2023).

[47] T. S. Parvini, E. Paz, T. Böhnert, A. Schulman, L. Benetti, F. Oberbauer, J. Walowski, F. Moradi, R. Ferreira, and M. Münzenberg, Enhancing spin-transfer torque in magnetic tunnel junction devices: Exploring the influence of capping layer materials and thickness on device characteristics, J. Appl. Phys. **133**, 243902 (2023).

[48] J. J. Bean, M. Saito, S. Fukami, H. Sato, S. Ikeda, H. Ohno, Y. Ikuhara, and K. P. McKenna, Atomic structure and electronic properties of MgO grain boundaries in tunnelling magnetoresistive devices, Sci. Rep. **7**, 45594 (2017).

[49] J. J. Bean and K. P. McKenna, Stability of point defects near MgO grain boundaries in FeCoB/MgO/FeCoB magnetic tunnel junctions, Phys. Rev. Mater. **2**, 125002 (2018).

[50] T. Böhnert, R. Dutra, R. L. Sommer, E. Paz, S. Serrano-Guisan, R. Ferreira, and P. P. Freitas, Influence of the thermal interface resistance on the thermovoltage of a magnetic tunnel junction, Phys. Rev. B **95**, 104441 (2017).

[51] M. Kuepferling, S. Zullino, A. Sola, B. Van de Wiele, G. Durin, M. Pasquale, K. Rott, G. Reiss, and G. Bertotti, Vortex dynamics in Co-Fe-B magnetic tunnel junctions in presence of defects, J. Appl. Phys. **117**, 17E107 (2015).

[52] F. Bohn, G. Durin, M. A. Correa, N. R. Machado, R. D. Della Pace, C. Chesman, and R. L. Sommer, Playing with universality classes of Barkhausen avalanches, Sci. Rep. **8**, 11294 (2018).

[53] M.-W. Yoo, J. Lee, and S.-K. Kim, Radial-spin-wave-mode-assisted vortex-core magnetization reversals, Appl. Phys. Lett. **100**, 172413 (2012).

[54] W. F. Brinkman, R. C. Dynes, and J. M. Rowell, Tunneling conductance of asymmetrical barriers, J. Appl. Phys. **41**, 1915 (1970).

[55] S. Jung, H. Lee, S. Myung, H. Kim, S. K. Yoon, S.-W. Kwon, Y. Ju, M. Kim, W. Yi, S. Han, B. Kwon, B. Seo, K. Lee, G.-H. Koh, K. Lee, Y. Song, C. Choi, D. Ham, and S. J. Kim, A crossbar array of magnetoresistive memory devices for in-memory computing, Nature **601**, 211 (2022).

[56] E. Alpaydin and C. Kaynak, Optical recognition of handwritten digits, UCI Machine Learning Repository (1998).

[57] A. Momeni, B. Rahmani, B. Scellier, L. G. Wright, P. L. McMahon, C. C. Wanjura, Y. Li, A. Skalli, N. G. Berloff, T. Onodera, *et al.*, Training of physical neural networks, Nature **645**, 53 (2025).

[58] B. Scellier and Y. Bengio, Equilibrium propagation: Bridging the gap between energy-based models and backpropagation, Front. Comput. Neurosci. **11**, 24 (2017).

[59] N. Dal Cin, F. Marquardt, and C. C. Wanjura, Training nonlinear optical neural networks with Scattering Backpropagation, arXiv:2508.11750 (2025).

[60] K. Y. Guslienko, B. A. Ivanov, V. Novosad, Y. Otani, H. Shima, and K. Fukamichi, Eigenfrequencies of vortex state excitations in magnetic submicron-size disks, J. Appl. Phys. **91**, 8037 (2002).

[61] A. Vaswani, N. Shazeer, N. Parmar, J. Uszkoreit, L. Jones, A. N. Gomez, Ł. Kaiser, and I. Polosukhin, Attention is all you need, in *Advances in Neural Information Processing Systems*, Vol. 30 (2017) pp. 5998–6008.

[62] S. Hochreiter and J. Schmidhuber, Long short-term memory, Neural Comput. **9**, 1735 (1997).

[63] T. N. Kipf and M. Welling, Semi-supervised classification with graph convolutional networks, in *International Conference on Learning Representations (ICLR)* (2017).

[64] R. Khaddam-Aljameh, M. Stanisavljevic, J. Fornt Mas, G. Karunaratne, M. Brändli, F. Liu, A. Singh, S. M. Müller, U. Egger, A. Petropoulos, T. Antonakopoulos, K. Brew, S. Choi, I. Ok, F. L. Lie, N. Saulnier, V. Chan, I. Ahsan, V. Narayanan, S. R.

Nandakumar, M. Le Gallo, P. A. Francese, A. Sebastian, and E. Eleftheriou, HERMES-Core—A 1.59-TOPS/mm^2 PCM on 14-nm CMOS in-memory compute core using 300-ps/LSB linearized CCO-based ADCs, IEEE J. Solid-State Circuits **57**, 1027 (2022).

[65] M. Le Gallo, R. Khaddam-Aljameh, M. Stanisavljevic, A. Vasilopoulos, B. Kersting, M. Dazzi, G. Karunaratne, M. Brändli, A. Singh, S. M. Müller, *et al.*, A 64-core mixed-signal in-memory compute chip based on phase-change memory for deep neural network inference, Nat. Electron. **6**, 680 (2023).

[66] M. Davies, N. Srinivasa, T.-H. Lin, G. Chinya, Y. Cao, S. H. Choday, G. Dimou, P. Joshi, N. Imam, S. Jain, Y. Liao, C.-K. Lin, A. Lines, R. Liu, D. Mathaikutty, S. McCoy, A. Paul, J. Tse, G. Venkataramanan, Y.-H. Weng, A. Wild, Y. Yang, and H. Wang, Loihi: A neuromorphic manycore processor with on-chip learning, IEEE Micro **38**, 82 (2018).

[67] P. A. Merolla, J. V. Arthur, R. Alvarez-Icaza, A. S. Cassidy, J. Sawada, F. Akopyan, B. L. Jackson, N. Imam, C. Guo, Y. Nakamura, B. Brezzo, I. Vo, S. K. Esser, R. Appuswamy, B. Taba, A. Amir, M. D. Flickner, W. P. Risk, R. Manohar, and D. S. Modha, A million spiking-neuron integrated circuit with a scalable communication network and interface, Science **345**, 668 (2014).

[68] C. Frenkel, M. Lefebvre, J.-D. Legat, and D. Bol, A 0.086-mm^2 12.7-pJ/SOP 64k-synapse 256-neuron online-learning digital spiking neuromorphic processor in 28-nm CMOS, IEEE Trans. Biomed. Circuits Syst. **13**, 145 (2019).

[69] L. Liu, D. Wang, D. Wang, Y. Sun, H. Lin, X. Gong, Y. Zhang, R. Tang, Z. Mai, Z. Hou, Y. Yang, P. Li, L. Wang, Q. Luo, L. Li, G. Xing, and M. Liu, Domain wall magnetic tunnel junction-based artificial synapses and neurons for all-spin neuromorphic hardware, Nat. Commun. **15**, 4534 (2024).

[70] S. A. Siddiqui, S. Dutta, A. S. Tang, L. Liu, C. A. Ross, and M. A. Baldo, Magnetic domain wall based synaptic and activation function generator for neuromorphic accelerators, Nano Lett. **20**, 1033 (2020).

[71] K. M. Song, J.-S. Jeong, B. Pan, X. Zhang, J. Xia, S. Cha, T.-E. Park, K. Kim, S. Finizio, J. Raabe, J. Chang, Y. Zhou, W. Zhao, W. Kang, H. Ju, and S. Woo, Skyrmion-based artificial synapses for neuromorphic computing, Nat. Electron. **3**, 148 (2020).

[72] W. Wan, R. Kubendran, C. Schaefer, S. B. Eryilmaz, W. Zhang, D. Wu, S. Deiss, P. Raina, H. Qian, B. Gao, S. Joshi, H. Wu, H.-S. P. Wong, and G. Cauwenberghs, A compute-in-memory chip based on resistive random-access memory, Nature **608**, 504 (2022).

[73] H. S. Carslaw and J. C. Jaeger, *Conduction of Heat in Solids*, 2nd ed. (Clarendon Press, Oxford, 1959).

[74] U. Martens, T. Huebner, H. Ulrichs, O. Reimer, T. Kuschel, R. R. Tamming, C.-L. Chang, R. I. Tobey, A. Thomas, M. Münzenberg, and J. Walowski, Anomalous Nernst effect and three-dimensional temperature gradients in magnetic tunnel junctions, Commun. Phys. **1**, 65 (2018).

[75] F. T. O'Neill and J. T. Sheridan, Photoresist reflow method of microlens production Part I: Background and experiments, Optik **113**, 391 (2002).

[76] Z. Yang, L. Bauer, and Z. Jacob, Design of microlens arrays for thermal imaging with spintronic Poisson bolometers, arXiv:2512.12491 (2025).

[77] T. S. Parvini, M. M. Tehranchi, S. M. Hamidi, and S. Sarkarati, Kolakoski sequence as an element to radiate giant forward and backward second harmonic signals, J. Appl. Phys. **118**, 183108 (2015).

[78] T. S. Parvini, M. M. Tehranchi, and S. M. Hamidi, New generation of one-dimensional photonic crystal cavities as robust high-efficient frequency converter, Photonics Nanostruct. Fundam. Appl. **25**, 25 (2017).

[79] T. S. Parvini and M. Khazaei Nezhad, Magnetooptical properties of one-dimensional aperiodic magneto-photonic crystals based on Kolakoski sequences, Appl. Phys. B **128**, 194 (2022).

[80] A. Vansteenkiste, J. Leliaert, M. Dvornik, M. Helsen, F. Garcia-Sanchez, and B. Van Waeyenberge, The design and verification of MuMax3, AIP Adv. **4**, 107133 (2014).

Supplementary Files

This is a list of supplementary files associated with this preprint. Click to download.

- SM.pdf